Noise-induced sidebranching in the boundary-layer model of dendritic solidification

Roger Pieters
Physics Department, University of California, Santa Barbara, California 93106
(Received 10 June 1987)

Under certain circumstances, sidebranching in a dendrite may result from the selective amplification of noisy fluctuations in the tip region. This suggestion is based on numerical and analytical studies of the two-dimensional boundary-layer model with both kinetic and surface tension anisotropy. From the dynamical simulations, smooth steady fingers are observed above a critical anisotropy, below which the fingers are unstable. Noise added to a smooth steady tip gives sidebranching. A temperature estimate of the required noise indicates that thermal noise is a candidate. An analytic description of the response of the tail of the dendrite to a perturbation in the tip region is given and this analysis is compared to the numerical results. Comparison is also made to experiment as the undercooling and anisotropy are varied. Implications for the full model are discussed.

I. INTRODUCTION

There are many simple nonequilibrium systems which generate complex structures or patterns. Examples are found in solidification[1] and in the displacement of one fluid by another, in convective hydrodynamic instabilities[2] and in flame-front propagation.[3]

In dendritic solidification a treelike solid grows from an undercooled melt. These structures are typically composed of a trunk or parabolalike finger of solid growing into the liquid with sidebranches or spatially oscillating structures developing on the sides of this finger. It is the purpose of this paper[4] to examine the origin of the sidebranching. It is suggested that sidebranching may result from the amplification of noisy fluctuations at the tip and that thermal fluctuations may be adequate to explain the observed effects.

This proposal is explored with the boundary-layer model of solidification. Note that the full solidification problem—which involves a moving interface, heat diffusion, and nonlinear boundary conditions—turns out to be relatively difficult to solve.[5] This has motivated a variety of simplified models including the local geometrical model[6] (GM) and the boundary-layer model[7] (BLM).

Recent work has dealt with the trunk or overall shape of the dendrite and the velocity at which it grows.[8] This work is briefly summarized as follows. Key are the experiments in which the trunk is observed to have a unique velocity and tip curvature for a given undercooling of a material.[9] The geometrical and boundary layer models have provided important insights into this selection of a particular velocity. Numerical simulations of the GM and BLM give a finger when a small but finite anisotropy is included. This finger displays a unique velocity and tip curvature, independent of the initial shape and depending only on the undercooling and anisotropy.[6,7] The question has been how this unique tip velocity and curvature are selected. For both the GM and BLM it turns out that the solution of the steady-state or time-independent problem gives a smooth finger with the same velocity and tip curvature as observed in the time-dependent simulations.[6,10] The steady-state problem is peculiar: The surface tension acts as a singular perturbation and this results in a discrete set of fingerlike solutions determined by a so-called "solvability condition" in which the anisotropy plays a crucial role. Of this set the finger with the highest curvature at the tip is the most physically reasonable and, indeed, this is the tip that emerges from the time-dependent numerical simulations. This correspondence between the steady-state solution and the dynamically selected finger is confirmed for the BLM by careful numerical work as will be described in Sec. II.

The peculiar character of the steady-state problem carries over to the full model in both two and three dimensions where again there is a solvability condition.[11] So, for the full model, it is reasonable to expect that the steady-state solution may again give the dynamically observed tip shape and velocity. This is currently under investigation.[12] Thus, the present understanding of the trunk—namely the overall shape of the finger and its growth velocity—is that it is given by the steady-state solution of the problem.

The second part of the problem, dealt with here, concerns the origin of the sidebranching behavior. One suggestion is that the tip region undergoes a dynamical oscillation which in turn results in sidebranching. Here the steady-state solution acts as the average shape about which the dynamics oscillates. There is limited evidence of tip oscillation under certain conditions, usually related to low undercooling.[13] However, no tip oscillation is observed in the bulk of the experimental work.[9,14,15] It is proposed here that noisy fluctuations near the tip may be sufficient to trigger the Mullins-Sekerka instability[16] of the relatively flat sides of the steady finger. The development of this instability then gives rise to the sidebranching behavior.

As mentioned, this suggestion of noise-generated sidebranching is based on work with the BLM. The BLM contains the essential physics yet, unlike the full model, it is simple enough that the simulations can be done readily. In Sec. II the BLM is described and numerical simula-

tions without noise are presented. It turns out that only a smooth steady finger emerges from the simulations. Initial transients do provide sidebranchlike behavior but, once the tip grows past these, only a smooth steady tip is produced. In addition, no dynamical oscillation of the tip is observed. It also turns out that these fingers are only stable above a critical anisotropy, where stability is in reference to the frame moving with the tip. The stability was determined heuristically from the dynamical simulations in the following way. A perturbation is applied to the tip and results in a growing and spreading instability on the side of the finger. This instability looks like a wave packet and resembles initial sidebranching behavior. Indeed, this is expected, since the relatively flat sides of the finger are unstable to the classic Mullins-Sekerka instability. However, above a critical anisotropy, the tip will outrun the developing instability, leaving a smooth steady tip. Hence, in the moving frame, the tip is stable.

To observe persistent sidebranching, the Mullins-Sekerka instability on the side of the finger needs to be continually triggered. One possibility is that thermal noise in the tip region may be adequate to trigger the instability of the sides of the dendrite. This possibility and an estimate of the required temperature are discussed in Sec. III. In Sec. IV dynamical simulations with noise along the dendrite are described. The distance from the tip at which sidebranching emerges is compared to those measured from experiment. An analytic description of the response of the tail of the finger to a perturbation at the tip is found in Sec. V. In Sec. VI this description is compared with the numerical results. Finally, in Sec. VII further experimental results are discussed and the implications for the full problem are explored.

II. DYNAMICAL SIMULATIONS

The boundary layer model[7] was devised to provide a simplified but physically reasonable model of solidification in two dimensions. In this problem a liquid is cooled below freezing by a temperature $\delta T = T_m - T_\infty$, where T_m is the melting temperature and T_∞ is the temperature of the undercooled liquid far from the solid. A dimensionless temperature can be defined as $u = (T - T_\infty)/(L/C_v)$, where C_v is the specific heat and L is the latent heat of fusion. Then undercooling is characterized by the dimensionless parameter $\Delta = (T_m - T_\infty)/(L/C_v)$ and the region of interest corresponds to $0 < \Delta < 1$. In this region excess latent heat piles up at the interface as solidification proceeds. The diffusion of this excess heat away from the interface controls the problem. As $\Delta \to 1$ the quantity of excess heat becomes small and so the heat forms a relatively thin layer along the interface. In this limit of $\Delta \lesssim 1$, the problem can be simplified by making the heat in this thin layer a function of the position along the interface and by then approximating the diffusion of heat normal to the interface.

The first step is to recognize that in two dimensions the interface between a solid and a liquid is just a curve or string. Given the normal velocity along the interface, the motion of this string is completely determined from geometrical considerations. The task is then to write an equation describing the evolution of the normal velocity and the thin layer of heat to which it is related.

To proceed, the interface can be described by $\kappa(s)$, the curvature as a function of arclength. Here $\kappa(s) = \partial\theta/\partial s$ where θ is the angle between an external fixed axis and the normal to the interface as shown in Fig. 1. The normal velocity of the interface, $v_n(s)$, determines the motion of the string in time through,

$$\left[\frac{\partial \kappa}{\partial t}\right]_n = -\left[\kappa^2 + \frac{\partial^2}{\partial s^2}\right] v_n \ , \tag{2.1}$$

and

$$\left[\frac{ds}{dt}\right]_n = \int_s k v_n ds \ . \tag{2.2}$$

The next step is to determine $v_n(s)$.[7,17] First, the excess latent heat accumulates in a layer at the interface. If the characteristic thickness of this layer of heat is small compared to the radius of curvature of the interface, then the heat layer can be approximated by the heat per unit length $h(s)$, which is a function only of arclength. Using $h(s)$, the temperature gradient at the interface can then be approximated. Finally, this normal gradient of the heat is related to $v_n(s)$ using the conservation of heat at the boundary. These steps give

$$v_n = \frac{w^2}{h} \ , \tag{2.3}$$

where $w = u_s/\Delta$ and u_s is the dimensionless temperature at the interface. Intuitively, the velocity of the interface increases as the layer of heat becomes smaller. See Ref. 7 for details.

The evolution of the heat $h(s)$ in time can be written as

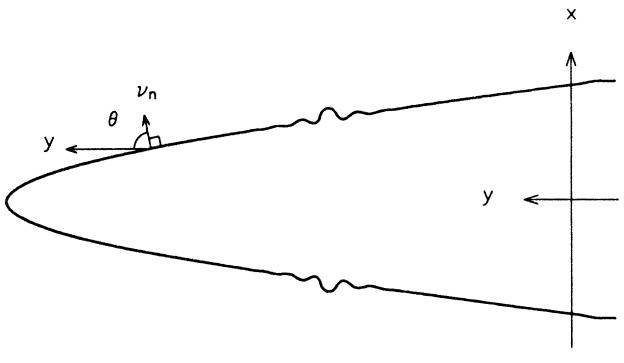

FIG. 1. The finger in xy at $t = 2000$ for $\Delta = 0.75$, $A_1 = 0.1$, and $\alpha = 0.0$. A single bump was made to the tip at $t = 0$. The resulting instability packet can be seen in the middle of the finger. A plot of this finger in $\kappa(s)$ is given in the last frame of Fig. 2. Only half the finger was run in the simulations and the finger was then reflected about the tip to give this picture. Note the definition of θ as the angle between the external axis y and the normal velocity v_n.

$$\left[\frac{\partial h}{\partial t}\right]_n = v_n(1-\Delta w) - v_n h\kappa + \frac{1}{\Delta^2}\frac{\partial}{\partial s}\left[\frac{h}{w}\frac{\partial w}{\partial s}\right], \quad (2.4)$$

where the terms on the right-hand side give, first, the heat added to the boundary through formation of solid; second, a geometrical term describing how the heat layer thins out as the interface is curved; and finally, a term giving the diffusion of heat along the boundary.

The temperature at the interface is given by

$$w = \frac{u_s}{\Delta} = 1 - \Delta^2 A(\theta)\kappa - \beta(\theta)v_n \ . \quad (2.5)$$

The first two terms on the right-hand side result from the Gibbs-Thomson relation. The equilibrium melting temperature is modified by the surface tension through the curvature κ. The surface tension can depend on the orientation of the interface, reflecting the anisotropy of the crystalline solid. Here $A(\theta)=1-\alpha\cos(4\theta)$ where a fourfold symmetry is assumed. However, this Gibbs-Thomson result is for a solid and liquid at equilibrium, while here the two are not quite in equilibrium because solid is forming at a finite rate. From simple kinetic arguments a small temperature difference is needed to drive solidification. In its simplest form this temperature difference is linearly proportional to the velocity.[18] Further, the kinetic coefficient β can depend on direction, again due to crystalline anisotropy. In the simulations reported here $\beta(\theta)=\Delta^4 A_1[1-\cos(4\theta)]$.

Note that (2.5) assumes only a slight deviation from equilibrium as represented by the small, linear kinetic term. This is valid for low undercooling. This region of low undercooling is also where most of the careful experimental work has been done. However, the approximations in the BLM hold for $\Delta \lesssim 1$. In this region growth velocities are large, the interface is far from equilibrium, and kinetic effects begin to play an important role. Indeed, in experiments at high enough undercoolings, kinetic effects rather than the diffusion of heat control the problem. Nevertheless, the BLM can be seen as an approximation to the experiments done at low undercooling. While this and other limitations are recognized, the goal is to provide a simple model whose qualitative features can be explored in an attempt to gain insight into the full problem.

The above equations were written in dimensionless form, where lengths are in units of d_0/Δ^3 and times are in units of $d_0^2/D\Delta^8$, where d_0 is the capillary length and D is the diffusion constant; see Ref. 7 for details. In Sec. VI a further step is taken to units where distances are scaled by the tip radius κ_t and times are scaled by the time for the tip to move one tip radius $1/\kappa_t v_t$, where v_t is the velocity of the tip. Thus, in these scaled units, characteristic distances and times are of order unity.

The five equations, (2.1)–(2.5), for κ, s, v_n, h, and w were discretized along the arclength and in time and were solved using a Crank-Nicolson implicit scheme. Note that as the interface evolves, the spacing of s along the interface ds will not remain constant. Here the evolution of ds is given by (2.2), and, in the discretization of the equations for the implicit scheme, the intervals in s are allowed to vary in the future time step. Then after each time step the points were redistributed to reestablish a constant ds. Growth in the length of the interface is accommodated by an increase in the number of points. Solving for the future time step in the implicit scheme involves inverting a matrix of size $5ns$ on a side, where ns is the number of points along the interface. As is usual in this type of problem, the nonzero matrix elements lie in a band along the diagonal and the program was written to take advantage of this. As a check the velocity was eliminated by substituting (2.3) for v_n in the equations for κ, s, w, and h. This left four equations which were solved using the same numerical method. Both calculations gave essentially the same results, and for a typical run the tip velocities differed by only 0.04% after a scaled time of 12.

Note that only half a dendrite is run. The string runs from tip to tail and a zero slope boundary condition at the tip enforces reflection symmetry. In the figures the string was reflected about an axis through the tip to provide a complete finger.

Before turning to the simulations, some comment should be made on how noise will eventually be added to the finger. The finger is bumped by making a small change in the appropriate fields between time steps. In order to determine the appropriate changes note that of the BLM equations, (2.1)–(2.5), only three are differential equations; (2.3) and (2.5) are relations. Thus there are only three independent initial conditions and applying a small perturbation to, say, the velocity requires a corresponding perturbation of h and w as well, which can be calculated from (2.3) and (2.5). In this way v_n, κ, and s are the independent fields. If the perturbation is not applied in this consistent manner and only one field is bumped, then high-frequency oscillations are introduced. Also, the perturbations should have a width of a few ds. Here the perturbative bump is taken to be a Gaussian of width $2ds$.

Note that a single bump applied to the tip takes a relatively long time to damp out. For the parameter region explored, the scaled time for the perturbation in the velocity to decay to one half of its maximum is from 2 to 20. Also the tip is excitable in that the change in the velocity becomes even larger than the initial jump. Overall then, the tip region is quite sensitive to perturbations.

The above procedure for bumping the tip assumes that a perturbation takes place in the full heat layer. Indeed this is one of the consequences of the BLM simplification. Recall that it was assumed that the heat layer was thin compared to the radius of curvature of the interface and hence the slice of heat normal to the interface was treated all at once through the variable $h(s)$. More realistically, when the heat layer becomes thick in the tail, a perturbation in the interface could occur without affecting the part of the heat boundary that is a distance far from the interface. Thus the BLM somewhat overestimates the coupling of the heat layer to the dynamics of the interface.

Finally, because of the character of the BLM, distant parts of the interface interact only through the thin boundary of heat along s. Thus the interface can cross itself and, indeed, this occurs in the indentations or

grooves that develop. This results in regions of high curvature which quickly become unphysical and force the simulations to end. Thus, for the BLM as described, only initial sidebranching behavior can be observed.

Turn now to the simulations which will be the focus of the rest of this section. In summary, first, anisotropy is required to form a finger. Second, it turns out that initial transients and numerical noise can provide sidebranchlike behavior on this finger but once these have been dealt with carefully, it is clear that only a smooth steady finger is produced. Third, the stability of the finger is determined heuristically by bumping the tip and observing the resulting wave packet on the side of the finger. It turns out that the finger is stable above a critical anisotropy. Finally, observing this wave packet leads naturally into a consideration of sidebranching.

First, anisotropy is required. In simulations without anisotropy, the tip slows and flattens, which is the first sign of tip splitting. Thus a seaweedlike structure is expected for no anisotropy.[7,19] However, when a moderate anisotropy is added, a steady tip forms. This moderate anisotropy will be quantified in the discussion below. The crucial role of anisotropy in forming a fingerlike structure is confirmed by the work on the steady-state problem where a finite anisotropy is needed in order to obtain a fingerlike solution.[10]

Second, it is important to ensure that the observed sidebranching is not a numerical artifact. Previous simulations with a moderate anisotropy began with either a semicircle or an Ivantsov parabola.[7] A smooth parabolic tip emerged having the shape and velocity of the selected steady-state solution. Recall that the selected solution is determined from the time-independent equations; for details, see Ref. 10. However, the development in the tail of deep cusplike grooves with large negative curvatures prevented the simulations from being run for long times. While this gave what looked promising sidebranch activity, the present simulations indicate that the grooving is just a result of the initial transient as the selected shape is sought out by the dynamics.

To see this and to explore longer times the selected shape—determined from the time-independent equations—was used as the initial condition. Again this was done for moderate anisotropies, where either the kinetic anisotropy, A_1 with $\alpha=0$, or the surface tension anisotropy, α with $A_1=0$, was used. In the following description, behavior with the kinetic anisotropy is given but the same results hold for simulations with surface tension anisotropy.

Because the dynamical simulations are discretized with a finite dt and ds, there is a small mismatch between the selected shape and the actual shape chosen by the simulation. The tip velocity chosen by the simulations is at most a few percent lower than the selected velocity and as dt and ds are reduced this mismatch decreases. Thus the correspondence between the dynamically selected finger and the steady-state solution is confirmed.

The simulations, starting with the selected shape, were run as far as possible and the grooving, which was initiated by the mismatch, was truncated. The resulting tip was then run and no further instabilities developed in the tip region. This confirms that the observed grooving results from initial transients.

However, even in these more careful simulations, some oscillation or corrugation in $\kappa(s)$ remains far down the tail. This corrugation again looks like emerging sidebranches far down the otherwise smooth finger. The amplitude of the corrugation grows with increasing arclength and eventually a given simulation ends as grooving develops. It turns out that this distant sidebranch corrugation is a numerical artifact. This was seen by measuring the arclength s_N at which this corrugation reached a given height of, say, 4% of the tip curvature. This limiting distance remains relatively constant for successive runs with the same ds and dt. However, the distance grows as ds and dt are reduced. That is, corrugation of a given height moves back from the tip as the simulations are made more accurate.

This corrugation is just sidebranching activity triggered by noise. The noise is generated in the numerical scheme by truncation error. As ds and dt are reduced the discretization error becomes smaller and the resulting noise is decreased. Starting with a smaller noise level requires a longer distance for this noise to be amplified to a given height. Thus, s_N increases as ds and dt are reduced. As will be seen below, this is the same mechanism that is proposed for the generation of sidebranching, except that the noise is thermal in origin.

As an example of this numerical noise consider $\Delta=0.9$, $\alpha=0.1$, and $A_1=0.0$. The tip velocity and curvature are $v_t=0.3410$ and $\kappa_t=4.975\times10^{-2}$ and the characteristic time and distances are, respectively, $\tau=1/\kappa_t v_t=59.0$ and $\rho_t=1/\kappa_t=20.1$. For $ds=0.10\rho_t$ and $dt=0.068\tau$, s_N is approximately $10\rho_t$. For runs with ds and dt both half of this, s_N becomes $17\rho_t$. Note that it would seem reasonable for ds and dt to be a tenth of the characteristic length and time scales, respectively. However, this leaves only a distance of $10\rho_t$ back from the tip at which the numerical noise results in reasonably small effects. Thus to simulate the BLM accurately for long times requires a considerable number of points and time steps. Thus, again, the finger appears to be a delicate structure in its sensitivity to numerical noise. And, in the same way, it is likely that considerable accuracy will also be necessary in the simulation of the full model.

With this careful treatment of the initial transients and the numerical noise, it is clear that steady smooth tips emerge from the dynamical simulations for moderate anisotropy. The third conclusion is that these smooth steady tips are stable for all anisotropies above a critical value. The stability of these fingers was observed by making a small perturbation to the tip. If one of the smooth steady tips is bumped once, by making a small consistent change in three of the fields as described earlier, an instability will develop. The instability manifests itself in the form of a small wave packet on the side of the finger and this packet grows and spreads. The development of this instability in $\kappa(s)$ is shown in Fig. 2 for $\Delta=0.75$, $A_1=0.1$, and $\alpha=0.0$. The tip, which is at $s=0$, has a velocity v_t and curvature κ_t of 0.2703 and 9.102×10^{-2}, respectively. Here the tip was bumped at $t=0$ by making a consistent change in the v_n, h, and w

fields at the tip. Here the velocity field was changed by a factor of 0.01. Note the xy plot corresponding to $\kappa(s)$ at $t=2000$ was given in Fig. 1. In the frame moving with the tip, the packet moves away from the tip at about the tip velocity and thus the instability is roughly stationary in the laboratory frame. See Sec. VI for more details.

As the simulation is continued, no further instability appears. Just a smooth tip with a steady velocity v_t is observed as the original grooving instability moves away, down the tail, in the moving frame. However, this packet is only swept out of the moving frame if it is not spreading too quickly. The center of the packet moves away from the tip at the tip velocity v_t. But the packet also spreads and each side of the packet acts like a front, moving out with a steady speed v_{front} relative to the center of the packet. Recall that the center of the packet is roughly stationary in the lab frame. For moderate anisotropy $v_{\text{front}}/v_t \ll 1$, the packet spreads slowly and the tip is

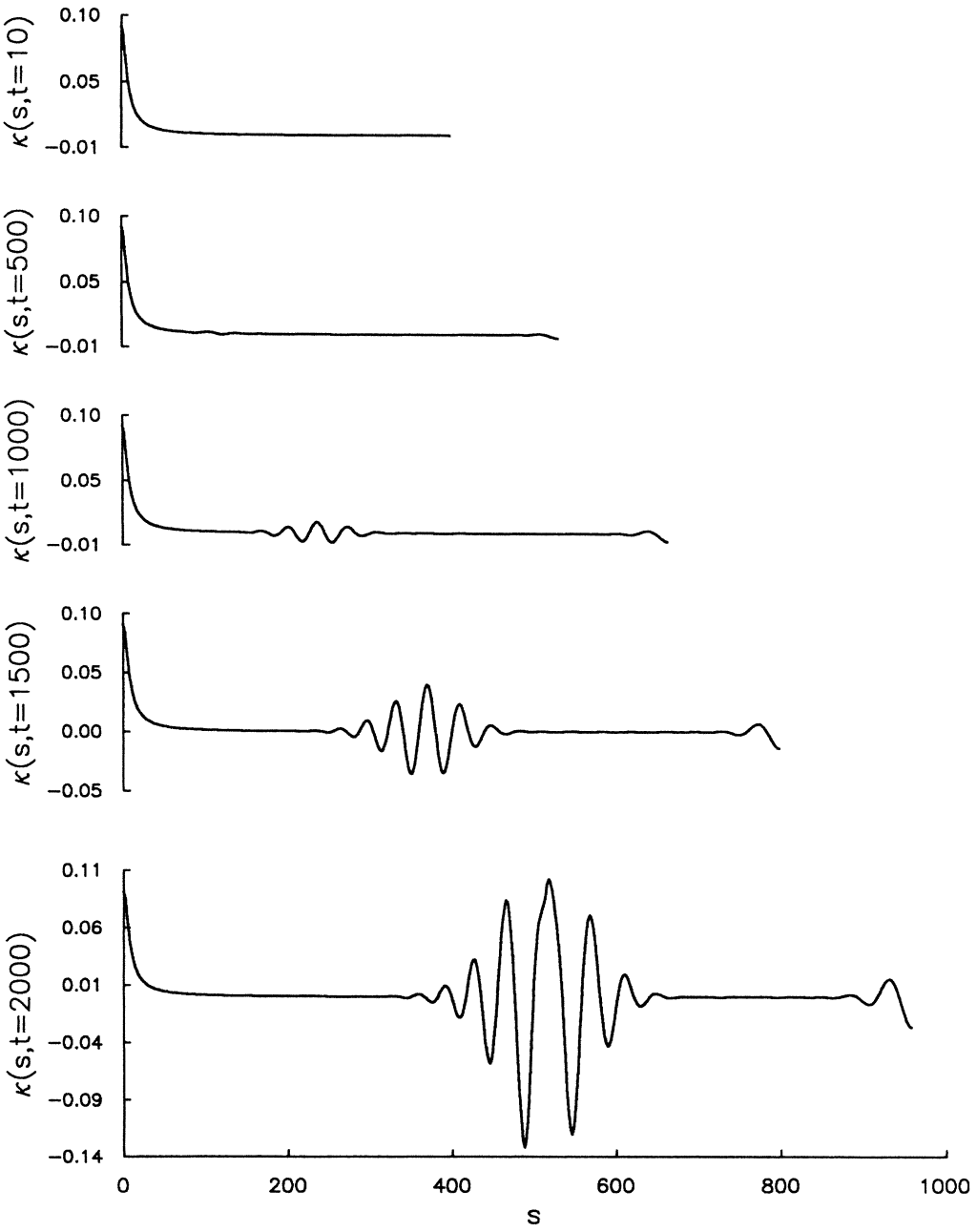

FIG. 2. The evolution of the finger in $\kappa(s)$ showing the development of the instability resulting from a single bump to the tip at $t=0$. Here $\Delta=0.75$, $A_1=0.1$, and $\alpha=0.0$ and $t=10$, 500, 1500, and 2000. These plots give the tip of the dendrite at $s=0$. The perturbation results in a packet which grows and spreads and moves back from the tip. Note that no further instability develops between the tip and packet.

stable. However, as the anisotropy is reduced, v_{front}/v_t increases and eventually becomes greater than one. Then the front spreads rapidly and encroaches on the tip. The front velocity was measured from the simulations and the critical anisotropy A_1^* at which $v_{\text{front}}/v_t = 1$ was determined. At the critical anisotropy A_1^* the front stays alongside of the tip. That is, even though the packet is moving away from the tip at the tip velocity v_t the packet is spreading at v_t and hence sidebranchlike activity stays alongside the tip. Below A_1^* the front encroaches on the tip and the tip is unstable. Fig. 3 gives a plot of the critical anisotropy as a function of Δ. In this way, the dynamical simulations indicate that, in the moving frame, the smooth needle fingers are stable above a critical anisotropy.

The critical anisotropy can also be seen in the behavior of the tip velocity v_t or, more sensitively, from the tip curvature κ_t as a function of time. Above the critical anisotropy the velocity and curvature of the tip are steady functions in time. Below A_1^*, v_t and κ_t oscillate with a growing amplitude as the instability pushes into the tip region. A similar behavior is observed in both the GM (Ref. 6) and in the GM modified to prevent the interface from crossing.[20] In both cases, a decaying (growing) oscillation of the tip curvature is observed above (below) the critical anisotropy for a given Δ.

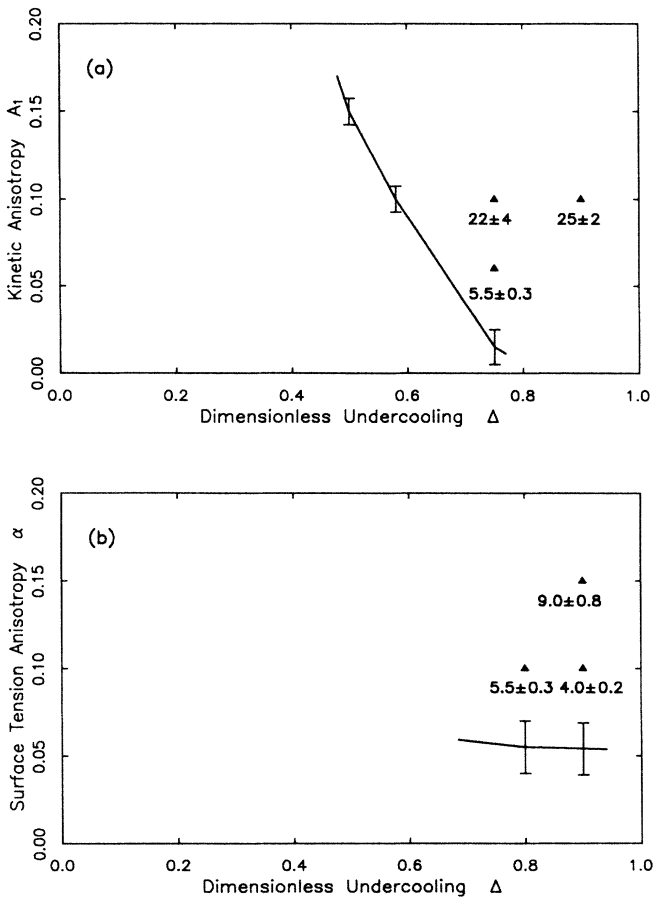

FIG. 3. The critical anisotropy is given by the solid line for (a) kinetic and (b) surface tension anisotropy. The error bars indicate the uncertainty in the critical anisotropy. The tip is stable for anisotropy and undercooling corresponding to points above this line. Tips corresponding to points below the line of critical anisotropy are unstable. σ_{SB} is given for the various parameter values marked by the solid triangles.

Thus below the critical anisotropy A_1^* the tip will be unstable, presumably to a tip splitting mode as observed in the simulations with no anisotropy. Only at A_1^*, which has a strong dependence on Δ, will the front remain alongside the tip to resemble sidebranching. However, experimentally, persistent sidebranching is observed over a large range of undercoolings for a given material and in a variety of materials with different anisotropies.

At this point there are several possibilities. First these local models may not be capturing the physics inherent in the three-dimensional experimental results. It may turn out that the sidebranchlike packet stays abreast of the tip for a range of anisotropies. However, this seems unlikely because the sidebranching packet is just a Mullins-Sekerka instability on a relatively flat interface and thus spreads at a specific velocity determined by the normal velocity of the side of the interface. It seems likely that the same picture will emerge for the full problem.

Second, sidebranching could be triggered through a small tip oscillation, as the tip velocity and curvature oscillate about some average value. However, no steady-state tip oscillation has been observed in either the GM or the BLM for $A_1 > A_1^*$. Nevertheless, both of these models are local in character and thus the full model may yet display the oscillation. For example, the sidebranching activity could effectively increase the radius of the tip, resulting in a reduced velocity. Further, from the experiments it is observed that the sidebranches recede from the tip as the velocity is reduced and this in turn could decrease the effective radius of the tip and hence increase the velocity. Thus, in a nonlinear fashion, the sidebranching and the tip radius could couple through the heat field to give a tip oscillation. This tip oscillation would in turn drive the sidebranching activity. This possibility must await a better understanding of the full model.

III. THERMAL NOISE

Another possibility, proposed here, is that thermal fluctuations near the tip may be adequate to trigger sidebranching. Thermal noise results in random fluctuations in the heat contained in a given volume. To introduce thermal noise, random changes were made in the thickness of the heat layer h. Recall from Sec. II that this requires corresponding changes in the velocity v_n and surface temperature w. The changes were made in the form of a Gaussian in s with width $2ds$ and centered on the tip, where ds is the spatial step in the discretization. Thus noise is only added to the tip; noise will be added along the dendrite in Sec. IV.

Focusing on the changes in velocity, thermal noise was modeled by making random changes in the tip velocity $\delta v_t/v_t = (2x_1 - 1)f_0$ at random time intervals $t = x_2 t_0$,

where x_1 and x_2 are random numbers between zero and one. Here f_0 gives the maximum change in the velocity and $t_0/2$ is the average time between changes. Corresponding changes were also made in h and w as described in Sec. II. Assuming that each random change δv_t affects the dendrite for a time dt, where dt is the time step in the simulations, and then squaring and averaging over time gives

$$\langle \delta v^2 \rangle = v_t^2 \frac{2}{3} \frac{dt}{t_0} f_0^2 . \tag{3.1}$$

The corresponding power spectrum is flat out to $\omega_c \simeq (dt)^{-1}$, which reflects the width of the perturbation in time. In the simulations dt is typically of order 0.05 in scaled units. Thus, effectively, the noise is white.

The changes in h and w which correspond to the change in velocity are given through (2.3) and (2.5),

$$\delta h = -\frac{\omega^2}{h^2} \delta v_n , \tag{3.2}$$

and

$$\delta w = -\beta(\theta) \delta v_n . \tag{3.3}$$

At the tip, $\theta = 0$, which gives $\beta(\theta) \propto 1 - \cos(4\theta) = 0$, and so changes in the surface temperature can be neglected in what follows.

The next step is to calculate the change in the dimensional energy δE caused by the change in the heat boundary δh. The energy in the heat boundary is given by

$$E = (T_s - T_\infty) C_v V = L u_s V , \tag{3.4}$$

where T_s is the temperature of the interface, T_∞ is the temperature of the undercooled liquid far from the interface, $u_s = (T_s - T_\infty)/(L/C_v)$ is the dimensionless temperature of the interface and V is the volume of the heat boundary.

Recall that the simulation is discretized in s. Effectively, the noise changes h in the interval ds at the tip. This change in h corresponds to changing the dimensionless volume $ds d_3 l$, where $l = h/(\Delta w)$ is the thickness of the heat layer[7] and d_3 is the thickness in the third dimension.

Recall that the BLM describes solidification in two dimensions. If we assume that the three-dimensional fingers observed in the experiments are described by making a solid of revolution out of the two-dimensional BLM, then at the tip $d_3 \simeq \pi ds$. A solid of revolution is not really satisfactory for the sidebranches because experimentally the sidebranches are not axisymmetric rings but modulate the "branching sheets" which point out from the main needle stem in four directions for fourfold symmetry.[14] However, the tip region is more or less axisymmetric and so this approximation is adequate for our estimate. Alternatively, in experiments which are effectively two dimensional, the dendrite is constrained between plates separated by a fraction of the tip radius ρ_t. Here d_3 would be the separation of the plates. Thus d_3 would again be of order ds for in the simulations $ds/\rho_t \simeq 0.1$.

The dimensional volume V is related to the dimensionless volume $ds d_3 l$ through

$$V = \left[\frac{d_0}{\Delta^3} \right]^3 ds d_3 l = \left[\frac{d_0}{\Delta^3} \right]^3 ds d_3 \left[\frac{h}{\Delta w} \right] . \tag{3.5}$$

Recall that in the BLM lengths are in units of d_0/Δ^3, where d_0 is the capillary length.[7] The energy, (3.4), in the boundary is changed by changing the volume,

$$\delta E = L u_s \delta V = L \left[\frac{d_0}{\Delta^3} \right]^3 ds d_3 \delta h . \tag{3.6}$$

Thus, through (3.6), δh, the dimensionless heat per unit length in the BLM is related to the dimensional energy. Note that ds, d_3, and δh are dimensionless; L is the latent heat of fusion.

Now recall

$$(\delta E)^2 = C_v k_B T^2 V , \tag{3.7}$$

where k_B is Boltzmann's constant and where again V is the dimensional volume and T is the temperature. Squaring (3.6), equating to (3.7), and using (3.1), (3.2), and (3.5) gives

$$T^2 = \left[\frac{L^2 d_0^3}{C_v k_B} \right] \left[\frac{2}{3} \frac{\pi}{\Delta^8} \frac{w_t^3}{\nu_t} \frac{ds^2 dt}{t_0} f_0^2 \right] , \tag{3.8}$$

where $w_t = 1 - \Delta^2 \kappa_t$ and where ν_t and κ_t are the velocity

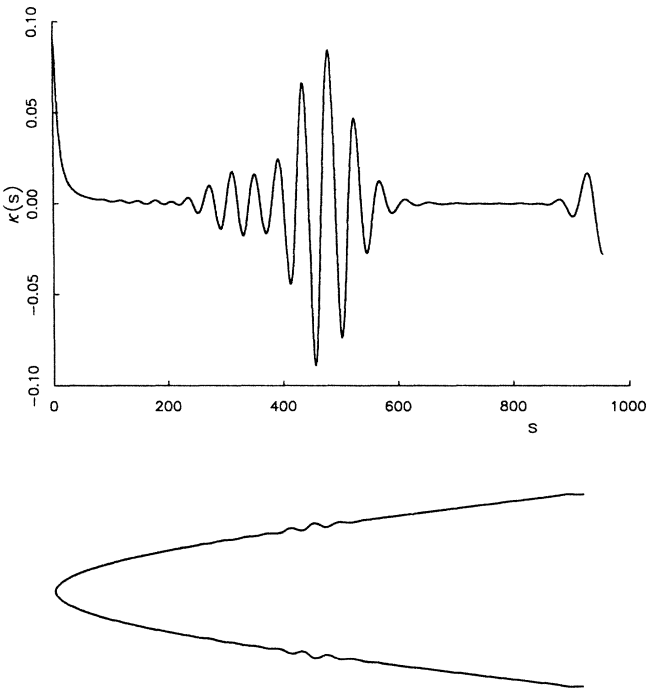

FIG. 4. $\kappa(s)$ and xy plot of a finger with noise added to the tip as described in the text. Here again $\Delta = 0.75$, $A_1 = 0.1$, and $\alpha = 0.0$ and $t = 2000$. This is the same finger as shown in Fig. 1 and in the last frame of Fig. 2 except that a stream of perturbations has been applied to the tip rather than a single bump. Note the continuous wave train emerging behind the tip in contrast to Fig. 2.

and curvature of the tip, respectively. The first group of dimensionless parameters is approximately 1.6×10^{6} K^2, where L, C_v, and d_0 are those of succinonitrile.[21]

The typical simulation is shown in Fig. 4. Notice the steady stream of sidebranching moving back from the tip in contrast to the finger shown in Figs. 1 and 2 where the tip was only perturbed once. Here $ds=1.0$, $dt=2.0$, $t_0=20$, $f_0=1.0\times10^{-4}$, $\Delta=0.75$, $A_1=0.1$, $\nu_t=0.2703$, and $\kappa_t=9.102\times10^{-2}$ and this gives $\simeq10^{-6}$ for the second factor. As a result, the temperature is on the order of a few degrees Kelvin, which is well below room temperature and the melting temperature of succinonitrile. Thus the dendrite is quite sensitive to small levels of noise. Admittedly, this estimate is crude but it does indicate that thermal noise may be adequate to account for the triggering of the sidebranches.

IV. THE EMERGENCE OF SIDEBRANCHING

In experiment, the distance back from the tip at which the sidebranches become significant varies with both the undercooling and the material parameters. Here these results are compared to those observed in the simulations of the BLM.

Sidebranching activity grows with increasing distance back from the tip and, indeed, it grows exponentially, as will be seen later. In order to quantify the emerging sidebranches, s_{SB} is defined as the distance from the tip at which the sidebranches reach some given height of, say, the tip radius. This distance along the arclength can be scaled by the tip radius,

$$\sigma_{SB}=\frac{s_{SB}}{\rho_t}=s_{SB}\kappa_t \ . \tag{4.1}$$

In scaled units, dendrites for different parameters have tip radii of unity and results can be compared directly.

For these simulations, thermal noise has been added along the dendrite, the noise strength being weighted by the thickness of the heat boundary. Recall that the fluctuations at a given temperature decrease as the volume is increased. Here it is assumed that a fluctuation must occur in the full heat layer for it to affect the dendrite. Since the heat layer becomes wider toward the tail, the volume increases and the likelihood of fluctuations decreases. Assuming a constant temperature, (3.8) gives the resulting noise strength along the dendrite,

$$f(s)=f_0\left[\frac{w_t}{\nu_t}\frac{\nu_n(s)}{w(s)}\right]^{3/2} \ . \tag{4.2}$$

Simulations with noise along the dendrite are essentially identical to those where noise was only added to the tip. This indicates, as expected, that it is the noise in the tip region that determines the structure in the tail.

At each of the discrete points along the interface the same procedure for adding noise was followed as used only at the tip in Sec. III, except now using $f(s)$ in place of f_0. Namely, in random time intervals, $t=x_1t_0$, the velocity at a point was bumped by $\delta\nu_n/\nu_n=(2x_2-1)f(s)$, where x_1 and x_2 are random numbers between zero and one and are chosen separately for each point along s. Corresponding changes were made to h and w as described in Sec. II.

In order to compare the values of σ_{SB} measured from fingers with differing values of Δ and A_1, the simulations were done with values of f_0 and t_0 that ensured that the dendrites were at the same effective temperature. In other words, the temperature T in (3.8) should be the same for all the simulations. Thus comparison of different values of σ_{SB} depends on the trustworthiness of the temperature estimates given by (3.8). Rather than running the simulations at a particular noise strength, it was more convenient to run the simulations at a variety of noise strengths f_0 corresponding to a variety of temperatures. Then σ_{SB} was measured for each temperature and the σ_{SB} for the desired temperature was interpolated by plotting log T^2 against $\sigma_{SB}{}^{1/4}$. This relation comes from (5.30) in the analytical work to be discussed.

Finally, the curvature $\kappa(s)$ shows the development of the sidebranching much more clearly than do the xy plots. As a result, it is more convenient to measure σ_{SB} from $\kappa(s)$ and care was taken to relate the $\kappa(s)$ results to what would be observed in the xy plots. Indeed, in the parameter region explored, this turns out to be straightforward and σ_{SB} was measured directly from the plot of $\kappa(s)$.

The measured values for σ_{SB} are given Fig. 3. There are two effects which can be observed. First, σ_{SB} decreases as the anisotropy is decreased at constant undercooling. This is as expected. Near the critical anisotropy the sidebranches begin to encroach on the tip and, below A_1, cause tip splitting. Second, σ_{SB} decreases as the undercooling is increased at constant anisotropy. In Fig. 3(a) increasing Δ from 0.75 to 0.9 at $A_1=0.1$ does not result in a decrease in σ_{SB} because of the compensating increase in distance from the critical anisotropy as the undercooling is reduced. However, in Fig. 3(b), increasing Δ from 0.8 to 0.9 does result in a decrease in σ_{SB}. In other words, the sidebranches move toward the tip as the undercooling is increased.

This second effect is also observed in the experiments of both Glicksman *et al.*[9,14] and Gollub.[22] Namely, as the undercooling is increased, the sidebranches emerge closer to the tip. However, as noted, the BLM is only valid for large undercooling and so comparisons with these experimental results for small Δ are made with some uncertainty. Nevertheless, the qualitative behavior of the BLM is encouraging.

V. ANALYTICAL DESCRIPTION OF SIDEBRANCHING IN THE TAIL

In the tail of the dendrite, the sidebranching can be described analytically as follows. Far down the tail the curvature will be small and so the steady-state solution can be approximated by an Ivantsov parabola,

$$\kappa=\nu_t(1-\Delta)\cos^3\theta \ . \tag{5.1}$$

The procedure will be to find the equations describing small deviations away from this solution. Solving these equations for a single perturbation at the tip results in a wave-packet-like disturbance on the side of the dendrite.

This packet is stationary in the lab frame and grows and spreads and shows good agreement with the wave packets observed in the simulations. Finally, from this, the waveform resulting from a sequence of noiselike perturbations is calculated.

To start, the equations will be written in terms of s, making s a large parameter which corresponds to being far down the dendrite. Note $s=0$ and $\theta=0$ at the tip. Next, convert to scaled units where distances are scaled by the tip radius, $\rho_t=1/\kappa_t$, and times are scaled by the time to move one tip radius, ρ_t/v_t. The purpose of this is to make characteristic times and distances of order unity so that structures can be compared directly. However, for convenience, instead of scaling with the actual tip radius, the radius of the corresponding Ivantsov parabola will be used, namely, $\rho_t^I=1/\kappa_t^I$, where $\kappa_t^I=v_t(1-\Delta)$. Another approximation to be used is that $s=0$ will be measured from the Ivantsov tip rather than from the actual tip. This approximation is reasonable in that the distance from the Ivantsov to the actual tip is at most a couple of tip radii in the parameter region explored. Finally, the effects of anisotropy in the tail region will be neglected.

Thus scaling gives

$$\sigma=(1-\Delta)v_t s$$

and

$$\tau=(1-\Delta)v_t^2 t \ ,$$

and as a result

$$\tilde{h}=(1-\Delta)v_t h, \quad \tilde{\kappa}=\kappa/[(1-\Delta)v_t]$$

and

$$\tilde{v}=v_t v_n \ ,$$

where the subscript on the normal velocity has been dropped. The equations for the BLM in the moving frame become

$$\left[\frac{\partial\tilde{\kappa}}{\partial\tau}\right]_\sigma=-\left[\tilde{\kappa}^2+\frac{\partial^2}{\partial\sigma^2}\right]\tilde{v}-\frac{\partial\tilde{\kappa}}{\partial\sigma}\int_0^\sigma\tilde{\kappa}\tilde{v}\,d\sigma' \ , \tag{5.2}$$

and

$$\left[\frac{\partial\tilde{h}}{\partial\tau}\right]_\sigma=\tilde{v}(1-\Delta\tilde{w})-\tilde{v}\tilde{h}\tilde{\kappa}+\frac{(1-\Delta)}{\Delta^2}\frac{\partial}{\partial\sigma}\frac{\tilde{h}}{\tilde{w}}\frac{\partial\tilde{w}}{\partial\sigma}-\frac{\partial\tilde{h}}{\partial\sigma}\int_0^\sigma\tilde{\kappa}\tilde{v}\,d\sigma' \ . \tag{5.3}$$

The normal velocity and surface temperature are given by

$$\tilde{v}=(1-\Delta)\frac{\tilde{w}^2}{\tilde{h}} \tag{5.4}$$

and

$$\tilde{w}=1-\Delta^2(1-\Delta)v_t A(\theta)\tilde{\kappa}-\beta(\theta)v_t\tilde{v} \ , \tag{5.5}$$

where $A(\theta)\simeq 1$ and $\beta(\theta)=0$ for neglect of anisotropy in the tail region.

In order to examine the sidebranching behavior, we do a linear perturbation analysis around the steady-state shape. In the limit of large σ, far down the tail, the steady-state solution becomes an Ivantsov parabola,

$$\kappa_0(\theta)=v_t(1-\Delta)\cos^3\theta \ , \tag{5.6}$$

which in scaled units becomes

$$\tilde{\kappa}_0(\theta)=\cos^3\theta \ . \tag{5.7}$$

To write the Ivantsov solution in terms of σ, use (5.7) in $\tilde{\kappa}=\partial\theta/\partial\sigma$. This gives

$$\sigma=\int_0^\theta\frac{d\theta}{\tilde{\kappa}}=\frac{\sin\theta}{2\cos^2\theta}+\tfrac{1}{2}\ln\left[\frac{1+\sin\theta}{\cos\theta}\right] . \tag{5.8}$$

For θ near $\pi/2$,

$$\sigma\simeq\frac{1}{2\cos^2\theta} \ , \tag{5.9}$$

which gives $\cos\theta\simeq(2\sigma)^{-1/2}$. As a result,

$$\tilde{\kappa}_0(\theta)=\cos^3\theta\simeq\left[\frac{1}{2\sigma}\right]^{3/2} , \tag{5.10}$$

$$\tilde{v}_0(\theta)=\cos\theta\simeq\left[\frac{1}{2\sigma}\right]^{1/2} , \tag{5.11}$$

and

$$\tilde{h}_0(\theta)=\frac{(1-\Delta)}{\tilde{v}_0}\simeq(1-\Delta)(2\sigma)^{1/2} . \tag{5.12}$$

Now perturb around the steady-state solution, $\tilde{\kappa}=\tilde{\kappa}_0+\tilde{\kappa}_1$ and $\tilde{h}=\tilde{h}_0+\tilde{h}_1$, keeping terms to first order in $\tilde{\kappa}_1$ and $\tilde{h}_1$. Further, keep only the terms which have coefficients of high order in σ, where σ is assumed to be large. After some algebra, the respective equations for $\tilde{\kappa}_1$ and $\tilde{h}_1$ become

$$\left[\frac{\partial}{\partial\tau}+\frac{\partial}{\partial\sigma}-\frac{2(1-\Delta)\Delta^2 v_t}{(2\sigma)^{1/2}}\frac{\partial^2}{\partial\sigma^2}+O(\sigma^{-5/4})\right]\tilde{\kappa}_1 = \left[\frac{1}{(1-\Delta)2\sigma}\frac{\partial^2}{\partial\sigma^2}+O(\sigma^{-9/4})\right]\tilde{h}_1 \ , \tag{5.13}$$

and

$$\left[\frac{\partial}{\partial\tau}+\frac{\partial}{\partial\sigma}+O(\sigma^{-1})\right]\tilde{h}_1 = -(1-\Delta)\left[1+v_t(1-\Delta)^2(2\sigma)^{1/2}\frac{\partial^2}{\partial\sigma^2}+O(\sigma^{-1/2})\right]\tilde{\kappa}_1 . \tag{5.14}$$

First, the third term on the left side of (5.13) can be neglected. Recall that σ is large and so this term will be smaller than the first two terms. A question that remains concerns the size of the $\partial^2/\partial\sigma^2$ factor. It will turn out that

$$\frac{\partial^2}{\partial\sigma^2}\propto q^2\simeq\omega_s^2\propto\sigma^{-1/2}\ ,$$

where q and ω_s are defined below. Thus the approximation of neglecting the third term is consistent. Note that by the same argument the first two terms on the right side of (5.14) are of the same order of magnitude and so both are retained.

Now set $\tilde{\kappa}_1$ and $\tilde{h}_1$ equal to $\exp[i\omega t+iW(\sigma)]$ and make the WKB approximation that

$$\frac{\partial^2}{\partial\sigma^2}(e^{iW(\sigma)})\simeq\left[i\frac{\partial W(\sigma)}{\partial\sigma}\right]^2 e^{iW(\sigma)}\ . \tag{5.15}$$

Defining $q=(\partial W/\partial\sigma)$ and solving gives

$$(\omega+q)^2=-\frac{q^2}{2\sigma}(1-\nu_t\epsilon^2\sqrt{2\sigma}q^2)\ , \tag{5.16}$$

where $\epsilon=(1-\Delta)$. This is a fourth-order equation in q and can be written as

$$\frac{\nu_t\epsilon^2}{\sqrt{2\sigma}}q^4-\left[1-\frac{1}{2\sigma}\right]q^2-2\omega q-\omega^2=0\ . \tag{5.17}$$

Recall that σ is large and thus $1/\sigma$ is a small parameter, making the quartic term a singular perturbation. The limit of $\sigma\to\infty$ gives two of the roots $q=\omega,\omega$, which become

$$q=\omega\pm[\text{small term of } O(\sigma^{-1/2})]\ ,$$

when σ is large. These are the roots of interest and will be examined in detail below.

The remaining two roots result from a dominant balance between the quartic and quadratic terms. Working to first order

$$q\simeq\pm\frac{(2\sigma)^{1/4}}{\nu_t^{1/2}\epsilon}\ , \tag{5.18}$$

and hence

$$W(\sigma)=\int q\,d\sigma\simeq\pm\frac{4}{5}\frac{2^{1/4}\sigma^{5/4}}{\nu_t^{1/2}\epsilon}\ . \tag{5.19}$$

Thus $e^{iW(\sigma)}$ corresponds to increasingly rapid spatial oscillations down the tail. These modes are highly stable and will not be considered further.

Returning to (5.16), solving for q and keeping terms to first order in the small parameter $\sigma^{-1/2}$ gives

$$q=\frac{\partial W(\sigma)}{\partial\sigma}\simeq-\omega\left[1\pm\frac{i}{\sqrt{2\sigma}}(1-\nu_t\epsilon^2\sqrt{2\sigma}q^2)^{1/2}\right]\ . \tag{5.20}$$

Thus to first order $q\simeq-\omega$. Making this substitution for q in the radical and integrating with respect to σ gives $W(\sigma)$ to first order in $\sigma^{1/2}$. Defining ϕ_σ gives

$$\begin{aligned}\phi_\sigma&=i\omega\tau+iW(\sigma)\\&\simeq-i\omega(\sigma-\tau)\pm\frac{2}{3}\left[\frac{1}{\nu_t\epsilon^2\omega}\right]\\&\quad\times[1-(1-\nu_t\epsilon^2\sqrt{2\sigma}\omega^2)^{3/2}]\ .\end{aligned} \tag{5.21}$$

Now the time dependence of $\tilde{\kappa}_1$ and $\tilde{h}_1$ will go as

$$\int A(\omega)e^{\phi_\sigma(\omega)}d\omega\simeq e^{\phi_\sigma(\omega)}\Big|_{\omega=\omega_s}\ , \tag{5.22}$$

where the method of stationary phase is used to approximate the integral. Here $A(\omega)$ is assumed to be flat in the region of interest and hence corresponds to a single, initial sharp perturbation in time. Here ω_s is determined by

$$\left.\frac{\partial\phi_\sigma}{\partial\omega}\right|_{\omega_s}=0\ . \tag{5.23}$$

For convenience in solving this equation convert to the variable $u=\nu_t\epsilon^2\sqrt{2\sigma}\omega^2$, where u is not to be confused with the dimensionless temperature of Sec. II. Then solving in powers of the small parameter $\sigma^{-1/2}$ gives for $u_s=\nu_t\epsilon^2\sqrt{2\sigma}\omega_s^2$,

$$u_s=\frac{\sqrt{3}}{2}\mp\frac{i(\sigma-\tau)}{4}\sqrt{3/2\sigma}+O(\sigma^{-1})\ . \tag{5.24}$$

Thus u_s is of order unity making ω_s^2 of order $\sigma^{-1/2}$ and hence the approximations discussed in connection with (5.13) and (5.14) are consistent.

From (5.21) the time dependence of $\tilde{\kappa}_1$ and $\tilde{h}_1$ can be obtained by substituting ω_s into ϕ_σ. First, using u_s,

$$\begin{aligned}\omega_s&=\left[\frac{u_s}{\nu_t\epsilon^2\sqrt{2\sigma}}\right]^{1/2}\\&\simeq\left[\frac{\sqrt{3}}{2\nu_t\epsilon^2\sqrt{2\sigma}}\right]^{1/2}\left[1\mp\frac{i(\sigma-\tau)}{2\sqrt{2\sigma}}\right]\ ,\end{aligned} \tag{5.25}$$

where again only terms to first order in $\sigma^{-1/2}$ are retained. Next, $1/\omega_s$ and $(1-\nu_t\epsilon^2\sqrt{2\sigma}\omega^2)^{3/2}=(1-u_s)^{3/2}$ are found in a similar fashion. Finally, substituting into $\phi_\sigma(\omega)$ gives the interesting result,

$$\phi_\sigma=\frac{1}{(1-\Delta)\sqrt{\nu_t}}\left[c_1\sigma^{1/4}\pm ic_2\frac{(\sigma-\tau)}{\sigma^{1/4}}-c_3\frac{(\sigma-\tau)^2}{\sigma^{3/4}}\right]\ . \tag{5.26}$$

The coefficients c_1, c_2, and c_3 are constants on the order of unity and are independent of any parameters. Defining $c_0=(1-\sqrt{3}/2)^{1/2}$, then $c_1=(2^{7/4}/3^{5/4})(1-c_0^3)$, $c_2=(3^{1/4}/2^{3/4})$, and $c_3=(3^{1/4}/2^{13/4})(1+c_0/2)$ or 0.810, 0.782, and 0.164, respectively.

Recall that the perturbation in the curvature and heat, $\tilde{\kappa}_1$ and $\tilde{h}_1$, due to a single disturbance at the tip is given by e^{ϕ_σ}. Thus from (5.26) this disturbance develops in the form of a wave packet which remains stationary in the lab frame. The third term of (5.26) gives the overall shape of the packet, which is just a Gaussian centered at $\sigma=\tau$. σ is measured from the tip and this means that the packet is moving back from the tip at unit velocity, which is just the tip velocity in the scaled units. Hence the packet is stationary in the lab frame. Also from the third term of (5.26), the width of the packet grows with increasing σ, namely, $\delta\sigma=(1-\Delta)^{1/2}\nu_t^{1/4}\sigma^{3/8}/c_3^{1/2}$. Thus the packet spreads as it moves back from the tip. The second term of (5.26) gives the wavelength with which the packet is modulated, $\tilde{\lambda}=2\pi(1-\Delta)\nu_t^{1/2}\sigma^{1/4}/c_2$,

which also increases gradually as the packet moves back. Finally the first term gives the overall amplitude of the packet, which grows as $\sigma^{1/4}$.

As discussed earlier, (5.26) describes the response of the dendrite to a single disturbance at the tip. Thus $\exp(\phi_\sigma)$ represents the Green's function. Taking the Fourier transform

$$G(\omega)=\int e^{\phi_\sigma} e^{i\omega\tau} d\tau \tag{5.27}$$

gives

$$|G(\omega)|^2 = G_c \exp\left[\frac{2c_1\sigma^{1/4}}{(1-\Delta)\sqrt{\nu_t}} - \frac{(\delta\sigma)^2}{4}\left[\omega-\frac{2\pi}{\lambda}\right]^2\right], \tag{5.28}$$

where G_c is some constant. Now

$$|\tilde{\kappa}_1(\omega)|^2 = |G(\omega)|^2 |\eta(\omega)|^2, \tag{5.29}$$

where $|\eta(\omega)|^2$ gives the power spectrum of the noise. From Sec. II, σ_{SB} is the scaled distance from the tip at which the sidebranching activity reaches a given amplitude in xy space or, in the parameter region explored, where $\kappa(s)$ reaches a scaled height $\tilde{\kappa}_0$. Thus the second result of interest,

$$\sigma_{SB} \simeq \frac{(1-\Delta)^4 \nu_t^2}{16 c_1^4} \ln^4(\tilde{\kappa}_0^{-2} G_c |\eta(\omega)|^2). \tag{5.30}$$

Here c_1, $\tilde{\kappa}_0$, and G_c are constants. From considerations similar to those in Sec. III, $|\eta(\omega)|^2$ is proportional to the factor $L^2 d_0^3/\kappa_B C_v T^2 \Delta^8$; for a related example see Ref. 23. With the temperature constant, σ_{SB} goes as $\nu_t^2 \ln^4(\Delta^{-8})$. Two trends are observed. First, the dependence of σ_{SB} on the velocity is consistent with what is observed in the simulations. Note that the velocity decreases as the anisotropy is reduced. At the same time the sidebranches emerge closer to the tip as the parameters move closer to the critical anisotropy. Thus σ_{SB} is observed to decrease as the velocity is reduced. On the other hand, while the velocity becomes larger with increasing Δ, the tip also becomes smaller and hence more sensitive to noise. This is reflected in the Δ^8 factor in (5.30). Thus (5.30) reflects the trends observed in the simulations.

VI. COMPARING ANALYTICAL AND NUMERICAL RESULTS

Equations (5.26) and (5.30) have been checked with the results from the dynamical simulations. First, for (5.26), this was done for various parameters; see Table I. For the remainder of this section the figures will only be shown for one choice of parameters, $\Delta=0.75$, $A_1=0.1$, and $\alpha=0.0$; the figures for the others are similar. The selected shapes, which have been run to remove the numerical mismatch as described in Sec. II, were used as the initial condition. Provided ds and dt are small enough, they will grow for long times maintaining the smooth selected shape. Here a single perturbation was applied to the tip by changing the velocity v_n at the tip by a small fraction. At the same time, h and w at the tip were changed to keep the equations consistent as described in Sec. II. As a result of this bump a small wave packet moves back from the tip, and this packet grows and spreads. Eventually, as the packet develops, the simulation comes to a stop due to grooving of the interface. Figure 2 is a plot of $\kappa(s)$ at a variety of times, showing the development of the wave packet. To analyze the wave packet, the extrema in $\kappa(s)$ were measured. These points define an outline of the packet and the spacing of these points determines the wavelength. The measurements on the outline of the packet and the wavelength were then converted to scaled units. Recall that s and t are arclength and time, which in scaled units become $\sigma=s/\rho_t$ and $\tau=t\nu_t/\rho_t$, respectively.

A. Velocity of the packet

First, the velocity of the packet was determined by measuring the position of the maximum in the outline of the packet as a function of time. There are two issues to address. One is to compare the position of the packet observed in the dynamical simulations to the analytical result. The second is to ask whether the packet is stationary in the laboratory frame.

The position of the maximum in the outline of the packet is plotted in Fig. 5. The measured velocity of the packet v_p for the various parameters is given in scaled units in Table I. From the analysis, as given by (5.26), the packet has a velocity of 1 and an intercept of 0, both given in scaled units and represented by the solid line in Fig. 5. First, the measured intercepts are all of the order of -1 in scaled units. These are small compared to the total run times on the order of 100. This small negative intercept probably results from the packet moving quickly through the highly curved tip region. Recall that the analysis is only valid for regions far from the tip and hence the intercept, from the analysis, is not expected to be correct. Next, note that the slope and hence the velocity of the packet v_p measured from the simulations is remarkably steady, even well into the regime where the packet begins to distort. The measured velocity is, however, consistently about 5% lower that the velocity given by the analysis. Remember that the analysis involves considerable simplification and small effects may have been neglected, a possible example of which is given below. Overall, then, there is reasonable agreement between the analysis and the simulations.

Now turn to the question of the velocity of the packet in the y direction. Note that the maximum in the packet is being measured in $\kappa(s)$. As the curve becomes articulated the arclength no longer provides a good measure of distance in xy from the tip. In other words, the measurements in $\kappa(s)$ are only legitimate for deformations which are small in xy space. Figure 1 shows a typical xy plot for the longest time considered. While the packet is clearly shown in $\kappa(s)$, it is barely visible in xy space and the approximation of using $\kappa(s)$ is reasonable. Further, it is assumed that $\theta \simeq \pi/2$, so that the packet is moving back almost parallel to the direction in which the tip is growing. Again from Fig. 1 this is reasonable. The actu-

TABLE I. A single bump applied to the tip of the finger results in an instability packet on the side of the dendrite. For three different fingers, various characteristics of the packet, which are predicted by the analysis, are compared to those measured from the simulations. See Sec. VI for more details.

Undercooling Δ	0.5	0.9	0.75
Kinetic anisotropy A_1	0.5	0	0.1
Surface tension anisotropy α	0	0.1	0
v_t	1	1	1
v_p	0.942±0.003	0.94±0.01	0.967±0.001
$\frac{1}{4}$	0.25	0.25	0.25
Slope of $\ln\langle\tilde{\lambda}\rangle$ vs $\ln\tau$	0.24±0.02	0.3±0.1	0.23±0.02
$\tilde{\lambda}_0$	1.91	0.46	1.04
$\tilde{\lambda}_0$ from intercept	2.04±0.2	0.97±0.2	1.34±0.3
Slope from (6.4)	3.304	13.66	6.180
Slope of $\ln\tilde{\kappa}_{\max}$ vs $\tau^{1/4}$	2.66±0.02	13.57±0.05	6.6±0.1
$\frac{3}{8}$	0.375	0.375	0.375
Slope of $\ln\delta\sigma$ vs τ	0.437±0.003	0.29±0.02	0.50±0.01
$\delta\sigma_0$	1.977	0.971	1.465
$\delta\sigma_0$ from intercept	2.35±0.03	1.4±0.2	1.42±0.04

al velocity is thus at most a few percent lower than the velocity measured from the arclength σ.

For the packet to be stationary in the lab frame, it should be moving back from the tip at the tip velocity v_t, which is one in the scaled units. The packet velocities v_p given in Table I are a few percent less than unity and when the approximations mentioned earlier are considered, the velocity at which the packet is moving back from the tip is about 10% less than the tip velocity. Note that measurement of the position of the two fronts—relative to the maximum in the packet—indicates that the packet remains quite symmetric. However, the

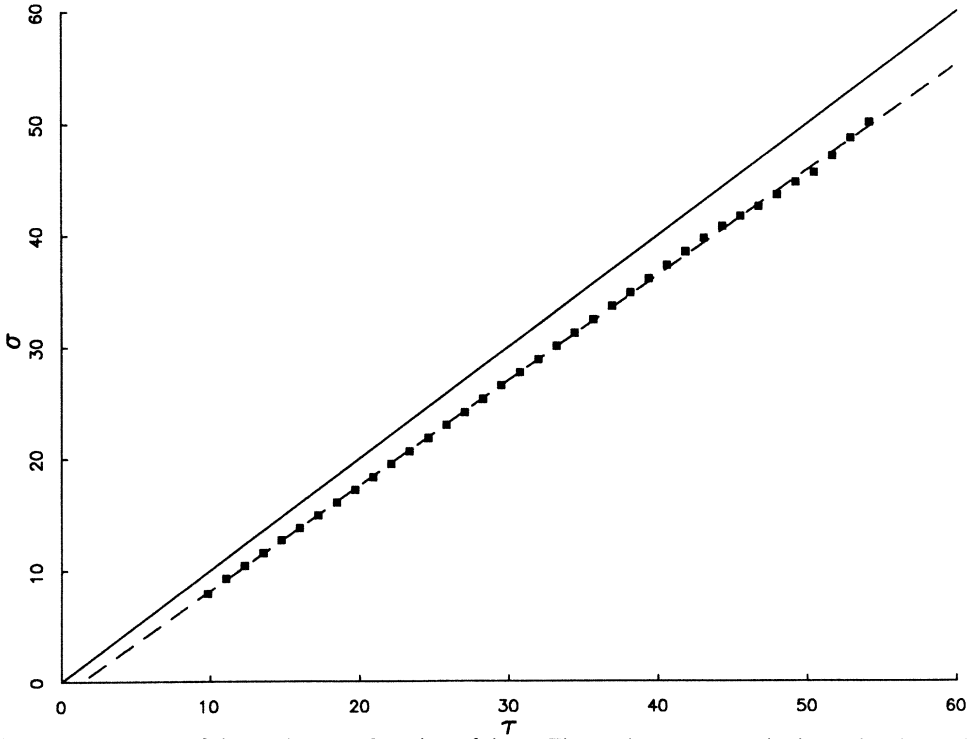

FIG. 5. The position of the center of the packet as a function of time. The packet measured is shown in Fig. 2. Here both position and time are given in scaled units. The slope determines the velocity of the packet v_p away from the tip. The solid line given by the analysis has a slope of unity, predicting that the packet moves back from the tip at the tip velocity v_t. The dashed line is the best fit through the data and has a slope v_p which is slightly less than one. For v_p see Table I.

growth rate on the side of the packet closest to the tip may be slightly higher than on the other side and this may tend to move the center of the packet toward the tip. Nevertheless, this effect is small. Thus the packet is roughly stationary in the lab frame, though it is being dragged along a bit by the tip.

B. Wavelength

Secondly, the wavelength of the packet was measured as a function of time. Recall that the predicted wavelength in scaled units is

$$\tilde{\lambda}=2\pi(1-\Delta)v_t^{1/2}\sigma^{1/4}/c_2 \ . \tag{6.1}$$

For convenience, set $\sigma=v_p\tau$, where v_p is the velocity of the center of the packet. Here v_p, as given in Table I, is approximately unity. Taking logarithms gives

$$\ln\tilde{\lambda}=\tfrac{1}{4}\ln\tau+\ln\tilde{\lambda}_0 \ , \tag{6.2}$$

where $\tilde{\lambda}_0=2\pi(1-\Delta)v_t^{1/2}v_p^{1/4}/c_2$.

In the simulations the wavelength is not constant within a packet. The center of the packet has the largest wavelength and the wavelength decreases on either side. This effect is absent from the analysis. The simulations are most likely beginning to grow out of the regime where the linear analysis holds. Indeed, the relative change of wavelength within a packet increases as the packet grows.

Since the packets are quite small, covering only a limited region of arclength, the wavelengths were averaged in each packet and in Fig. 6 $\ln\langle\tilde{\lambda}\rangle$ was plotted as a function of time. The error bars give the deviation for the wavelength within each packet. Note also that the wavelengths were measured out to 1% of the maximum peak height. Thus, as the packet grows, new wavelengths enter the measured packet and this gives the slight oscillation about the average which is observed in these plots. Alternatively, the wavelength of, say, the central peak can be used and similar results are obtained.

Table I provides the slope and the factor of $\tilde{\lambda}_0$ computed from the intercept. Note the considerable error in the slope and $\tilde{\lambda}_0$ for $\Delta=0.9$, $A_1=0$, and $\alpha=0.1$. From Fig. 3 this set of parameters is relatively close to the critical anisotropy and as a result the tip is more sensitive to noise and the packet grows relatively quickly. Hence the spread of the data points in time is smaller and the slope and intercept less well resolved.

The slopes clearly confirm to within 10% the exponent of 1/4 in σ with which the wavelength coarsens. The factor of $\tilde{\lambda}_0$ also shows reasonable agreement with the values of $\tilde{\lambda}_0$ predicted from the analysis, confirming the value of c_2 to within $\simeq 15\%$.

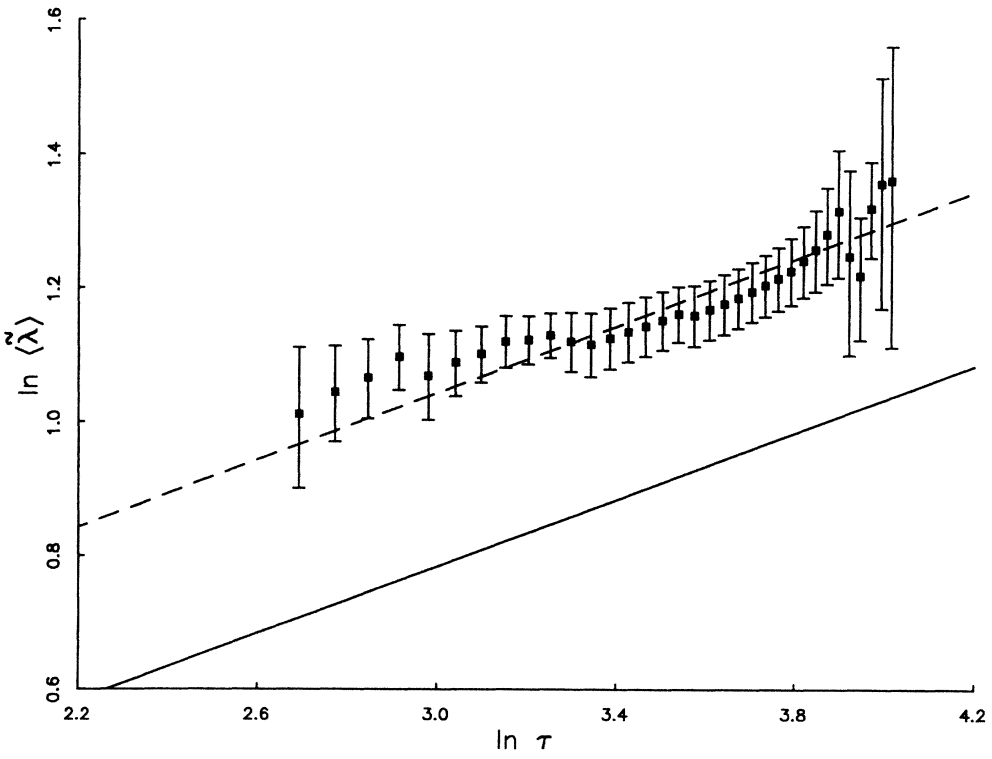

FIG. 6. The average wavelength of the interface inside the packet as a function of time. The packet measured is shown in Fig. 2. Again, both wavelength and time are in scaled units. The solid line is given by the analysis and the dashed line gives the best fit through the data. The solid line is shifted because of the slight error in both the intercept and slope of the data. Note the slope is clearly $\frac{1}{4}$, confirming the $\tau^{1/4}$ dependence predicted by the analysis.

C. Height

Equation (5.26) gives the height of the packet in $\tilde{\kappa}(\sigma)$,

$$\tilde{\kappa}_{\max}=C\exp\left[\frac{c_1}{(1-\Delta)\sqrt{\nu_t}}\sigma^{1/4}\right], \tag{6.3}$$

where C is some constant. Taking logarithms gives

$$\ln\tilde{\kappa}_{\max}=\frac{c_1\nu_p^{1/4}}{(1-\Delta)\sqrt{\nu_t}}\tau^{1/4}+\ln C\ . \tag{6.4}$$

The maximum height of the outline of the packet in $\tilde{\kappa}(\sigma)$ was measured and $\ln\tilde{\kappa}_{\max}$ was plotted against $\tau^{1/4}$ as shown in Fig. 7. In Table I the measured slopes are compared with those given by the analysis. Note that for later times the packet begins to distort, with the center of the packet becoming tall and narrow. This accounts for the upturn at longer times in Fig. 7. The distortion can also be seen in the last frame of Fig. 2. Note that for these longer times the amplitude of the instability is becoming large and the instability is moving beyond the regime where the linear analysis holds. Thus distortion in the packet is not unexpected as nonlinear effects begin to play a role.

The analysis predicts that the height of the packet will grow like $\sigma^{1/4}$. The fit between the data and the analysis as shown in Fig. 7 is good. However, the question is to what extent this data distinguishes between an exponent of 1/4 and another exponent of, say, 1/2 or 1. Here, plots of $\ln\kappa_{\max}$ against τ^a are reasonably straight for a in the range of 0.2–0.7. However, the good quantitative agreement of the measured slope with that from the analysis seems to be strong evidence in favor of having obtained the right analytical form.

D. Width at half height

For a Gaussian, $e^{-\alpha\sigma^2}$, the width at half height is given by $\delta\sigma=2\sqrt{\ln 2/\alpha}$. Using (5.26) to determine α gives

$$\delta\sigma=\delta\sigma_0\tau^{3/8}\ , \tag{6.5}$$

where

$$\delta\sigma_0=\left[\frac{4\ln 2(1-\Delta)\nu_t^{1/2}\nu_p^{3/4}}{c_3}\right]^{1/2}\ . \tag{6.6}$$

The width of the outline of the packet at half height was measured and $\ln\delta\sigma$ is plotted as a function of $\ln\tau$ in Fig. 8. Table I gives the slope and $\delta\sigma_0$ for the various parameters and compares them to the values predicted by the analysis. Note that the plots, as can be seen from Fig. 8, are quite straight. However, the measured values of the slope are not that close to the power of $\frac{3}{8}$ predicted by the analysis. Despite the relatively straight lines and the re-

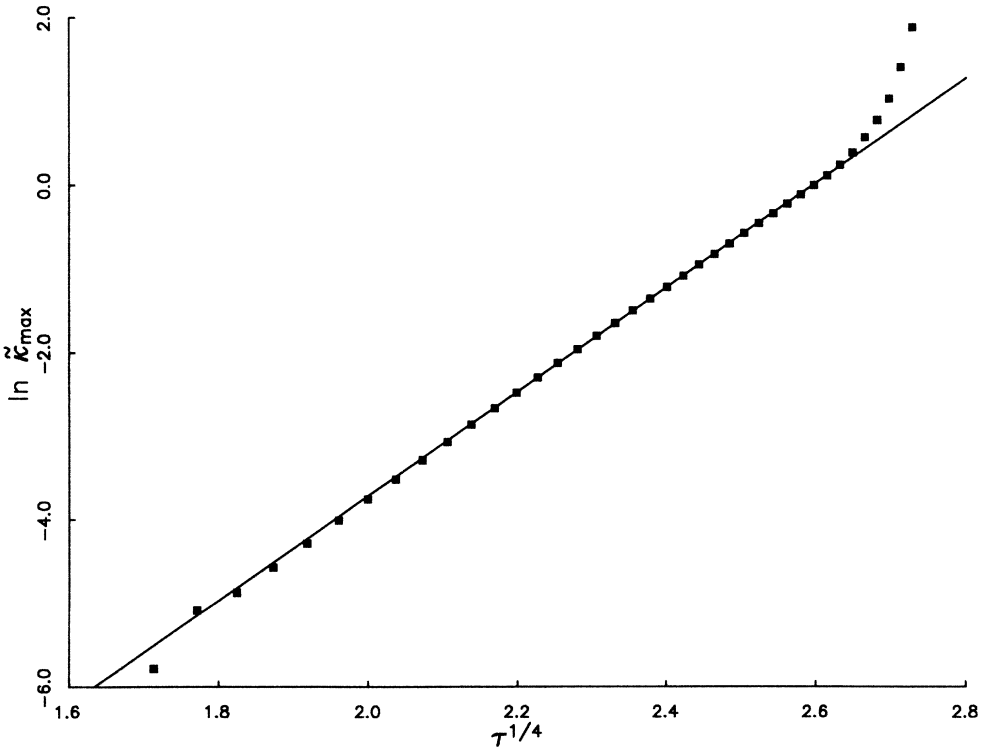

FIG. 7. The height of the maximum in the outline of the packed as a function of time. The packet measured is shown in Fig. 2 and the height and time are given in scaled units. The solid line gives the slope predicted by the analysis and is drawn with a convenient intercept. Note the good agreement of the slopes.

sulting small errors for the measured slope and intercept—here the error is given by a least-squares analysis of the data— the measurement of the width of the packet depends sensitively on the shape and height of the packet. As the packet develops it may be distorting slightly, thus resulting in a faster growth rate of the width than predicted by the analysis. Nevertheless, there is general agreement.

E. σ_{SB} as a function of f_0

The last four measurements have dealt with the instability packet resulting from a single perturbation of the tip. Now consider the wave train resulting from a stream of perturbations or noise acting on the tip. With the presence of noise, (5.30) gives σ_{SB}. Recall from Sec. II that σ_{SB} is the distance from the tip at which the side branching grows to a certain threshold, here taken to be one tip radius. σ_{SB} was measured for a variety of noise strengths f_0. From Sec. III the noise strength $|\eta(\omega)|^2$ is proportional to f_0^{-2}. Substituting into (5.30) gives

$$\sigma_{SB}=\frac{(1-\Delta)^4 v_t^2}{16c_1^4}\ln^4(Cf_0^{-2}) , \tag{6.7}$$

where C is some constant. Taking the fourth root,

$$\sigma_{SB}^{1/4}=-\frac{(1-\Delta)v_t^{1/2}}{2c_1}\ln f_0+\frac{(1-\Delta)v_t^{1/2}}{2c_1}\ln C . \tag{6.8}$$

Figure 9 is a plot of $\sigma_{SB}^{1/4}$ against $-\ln f_0$ for $\Delta=0.75$, $A_1=0.1$, and $\alpha=0$ with $t_0=20$ and f_0 from 5×10^{-2} to 5×10^{-5}. Here noise was added only to the tip; the slope remains essentially the same when noise is added along the whole dendrite. The measured slope is 0.174 ± 0.02 which compares well with $(1-\Delta)v_t^{1/2}/c_1=0.161$. Similar good agreement is obtained for a variety of other parameters, confirming the analytical result.

Overall, some difficulty is encountered in measuring both the shape of the packet resulting from a single disturbance at the tip and in measuring the σ_{SB} due to a stream of noiselike perturbations in the tip region. As mentioned, the shape of the packet is determined from the extrema in $\kappa(s)$. However, when the packet is small there are few extrema and this introduces uncertainty into the exact shape. But when the packet is larger and its overall shape is more readily determined, nonlinear effects begin to play a role. Also, the perturbation in the numerical simulations must first traverse the tip region while the analytical results deal only with large σ. Nevertheless, the agreement between the numerical simulations and the analytical work is reasonably good, indicating that the analytical results are capturing the initial sidebranching dynamics.

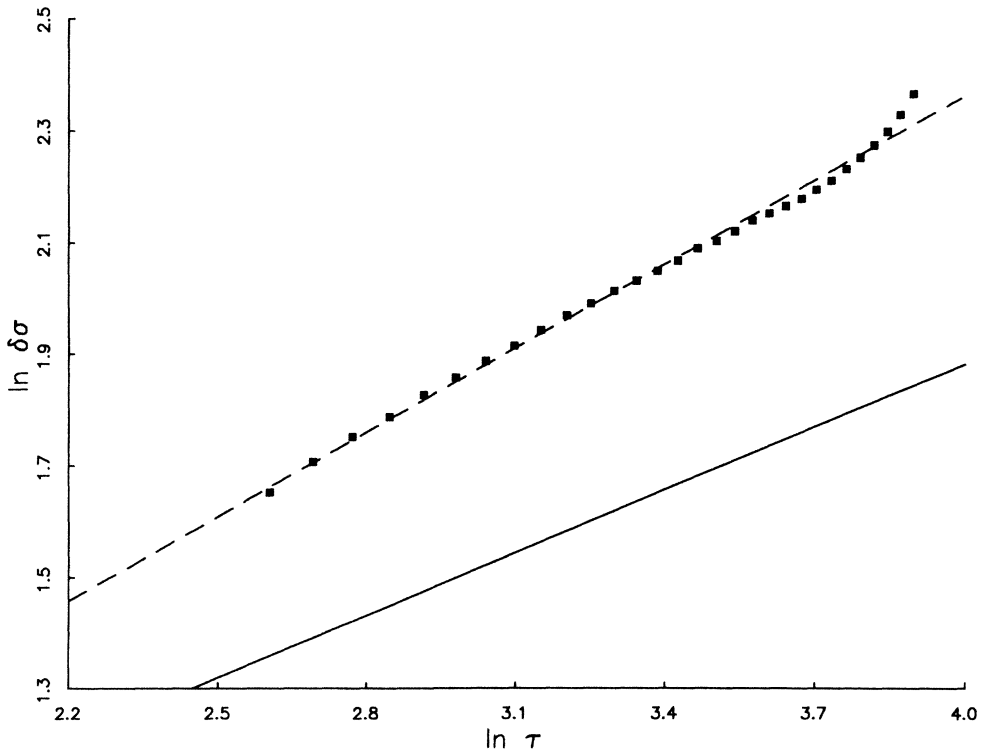

FIG. 8. The width of the packet at half height as a function of time. The packet measured is shown in Fig. 2 and the width and time are given in scaled units. The solid line is given by the analysis and the dashed line is a fit to the data. See Table I for the value of the slope and intercept.

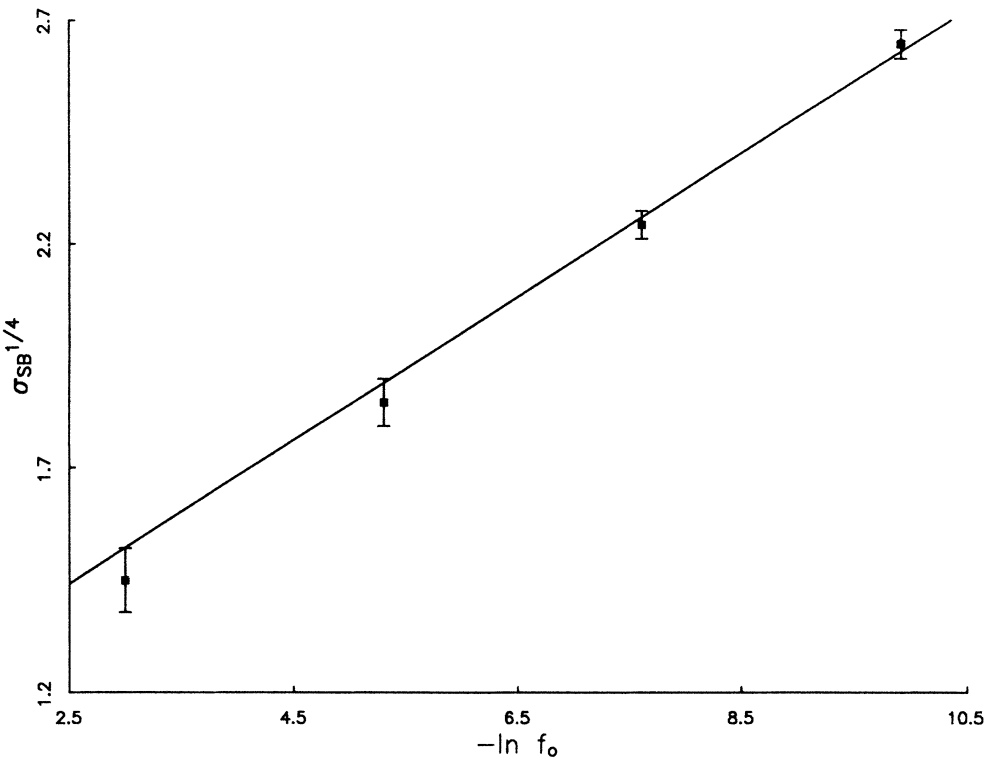

FIG. 9. $\sigma_{SB}^{1/4}$ as a function of $-\ln f_0$ for $\Delta=0.75$, $A_1=0.1$, and $\alpha=0.0$. Here f_0 is the noise strength and σ_{SB} is the distance from the tip at which the sidebranches reach a height of κ_t. The solid line gives the slope predicted by the analysis and is drawn with a convenient intercept.

VII. CONCLUSION

Experiment lends support to this picture of noise generated sidebranching. Considerable experimental work has been done by Glicksman *et al.*[9,14] and more recently by Dougherty *et al.*[15] on a single dendrite growing in an unconstrained environment and covering an extensive range of undercoolings. The velocity and radius of the tip and the sidebranching behavior have been carefully observed for these three-dimensional dendrites. The work by Dougherty *et al.*[15] resolves the solid-liquid interface with great accuracy and focuses on the sidebranching in the tip region.

First, no oscillation of the tip velocity is observed. Second, a plot of the amplitude of the sidebranching at a given distance back from the tip is oscillatory, but intermittent: The Fourier transform has a rather broad peak about a given wavelength. Thus, rather than simply observing steady, periodic sidebranching as would be expected with a tip oscillation, the sidebranching has intermittent breaks and shifts in the oscillating wave train. Third, with a tip oscillation, the sidebranching on opposite sides of the dendrite would tend to be correlated, especially near the tip. However, no significant correlation is observed. Finally, from the careful measurements made by Dougherty *et al.*,[15] the rms amplitude of the sidebranching is observed to increase exponentially from the tip and there is no apparent onset of sidebranching. These provide reasonable evidence for a noise-dependent mechanism.

Here, only thermal noise has been considered. Other types of noise are possible as well, such as fluctuations in the solidification rate or perturbations produced as defects are incorporated into the solid. Indeed a tip oscillation could itself act as a sort of regular perturbation which in turn continually triggers the MS instability in the tail, thereby giving rise to sidebranching. Or more speculatively, if the inherently nonlinear tip dynamics turns out to be chaotic in the parameter regime of interest, this too could provide the noise required for persistent sidebranching. This, of course, assumes that a dynamical tip oscillation would have a small amplitude and that it would act only to trigger the MS instability on the side of the finger. Alternatively, the oscillation could be large enough that its frequency would dominate in selecting the wavelength of the sidebranching and this would result in correlation of the sidebranching on the two sides of the dendrite.

While the bulk of experimental work confirms a noise-dependent picture, note should be taken of some—so far limited—experimental work under special conditions where noise amplification is clearly not the mechanism. First, dynamical oscillations have been reported for dendrites that are effectively two dimensional and grown at low undercooling.[13] In these experiments the dendrites are constrained between two glass slides which have a separation on the order of the tip radius. Regular dendrites are observed at higher undercoolings. As the un-

dercooling is reduced, a tip oscillation with periodic and correlated sidebranching is clearly observed. However, no systematic study of these oscillating states has yet been done. There remain uncertainties, such as the possibility of impurity effects, and there are also difficulties with experimental work at low undercooling because of the large diffusion length; see Ref. 1. The tip oscillation may be related to the instability of the tip described in Sec. II as the critical anisotropy, or here the critical undercooling, is reached. From Fig. 3, as the undercooling is reduced at constant anisotropy, the sidebranching spreads more and more quickly until, at the critical undercooling, the sidebranching spreads quickly enough to stay abreast of the tip and result in a tip oscillation. However, this occurs only at one specific undercooling. Detailed experimental work is needed for comparison.

Also, in directional solidification, as the many parallel cells begin to form into dendrites, there is a clear correlation of the emerging sidebranches across the field of view which includes tens of fingers.[24] Here, of course, the dendrites interact strongly with each other and this may provide a basis for a dynamical oscillation.

Thus the bulk of the experimental work with single, unconstrained, and hence three-dimensional dendrites supports the noise amplification mechanism. However, as mentioned, there is also preliminary evidence that, under certain conditions, dynamical oscillations are observed. This is not unreasonable. From the BLM it was seen that the tip is very sensitive to perturbations and this sensitivity can easily lead to both type of mechanisms.

Note that only initial sidebranching behavior has been explored. In experimental work, at about $10\rho_t$ from the tip, the sidebranching wavelength coarsens through competition. Here, some branches begin to slow down relative to neighboring branches and eventually they are left behind. This behavior is not dealt with by the analytic work which considers only small linear perturbations, nor by the numerical work as the approximations made in the BLM limit it to modeling a thin layer of heat. The thickness of this layer does not remain small relative to the curvature in well-developed sidebranching.

The main thrust here has been to examine the origin of sidebranching. This work with the BLM indicates that sidebranching emerges from the Mullins-Sekerka instability of the relatively flat sides of the finger and that this instability is triggered by noise in the tip region. In the frame moving with the finger, the instability resulting from a single perturbation of the tip moves back from the tip at roughly the tip velocity. This instability grows and spreads but, above the critical anisotropy, the instability spreads at a speed less than the velocity of the tip. Hence the instability moves out of the frame moving with the finger. For continuous sidebranching to be observed, the instability must be continually triggered by noise in the tip region. In other words the sidebranching pattern results from the selective amplification of noise. This concept of a pattern depending on noise has also been discussed in the context of the Ginzburg-Landau equation.[25]

Note that the packet observed on the side of the dendrite is remarkably similar to that observed on a plane. For example, the wavelength that emerges on the sides of the dendrite is within 15% of the wavelength of the fastest growing mode for a plane with the corresponding velocity. This means that the initial sidebranching on the dendrite is relatively easy to understand in an intuitive fashion in terms of the Mullins-Sekerka instability being triggered by noise. It seems reasonable to expect this to carry over to the full model.

ACKNOWLEDGMENTS

I am grateful for the help and support of J. S. Langer throughout this work. I wish to thank E. Ben-Jacob and N. Goldenfeld for providing computer codes and for general assistance in the initiation of this project. Also, I gratefully acknowledge the support granted by the Natural Sciences and Engineering Research Council of Canada and additional support from the Heritage Foundation of Alberta. This research was supported by the U.S. Department of Energy Grant No. DE-FG03-84ER45108 and in part by the National Science Foundation under Grant No. PHY-82-17853, supplemented by funds from the National Aeronautics and Space Administration, at the University of California, Santa Barbara.

[1]J. S. Langer, Rev. Mod. Phys. **52**, 1 (1980).

[2]D. Bensimon, L. P. Kadanoff, S. Liang, B. I. Shraiman, and C. Tang, Rev. Mod. Phys. **58**, 977 (1986); G. Ahlers, D. S. Cannell and V. Steinberg, Phys. Rev. Lett. **54**, 1373 (1985); C. W. Meyer, G. Ahlers, and D. S. Cannell, *ibid.* **59**, 1577 (1987).

[3]Ya. B. Zel'dovich, A. I. Istratov, N. I. Kidin, and V. B. Librovich, Combust. Sci. Technol. **24**, 1 (1980).

[4]This is an expanded version of work reported in R. Pieters and J. S. Langer, Phys. Rev. Lett. **56**, 1948 (1986).

[5]J. B. Smith, J. Comp. Phys. **39**, 112 (1981). Here the full model refers to either the one-sided or symmetric models as described in Ref. 1. See also Ref. 7.

[6]R. C. Brower, D. A. Kessler, J. Koplik, and H. Levine, Phys. Rev. Lett. **51**, 1111 (1983); Phys. Rev. A **29**, 1335 (1984); D. A. Kessler, J. Koplik, and H. Levine, *ibid.* **30**, 3161 (1984); **31**, 1712 (1985).

[7]E. Ben-Jacob, N. Goldenfeld, J. S. Langer, and G. Schön, Phys. Rev. Lett. **51**, 1930 (1983); Phys. Rev. A **29**, 330 (1984).

[8]For a review of recent work see J. S. Langer, in *Chance and Matter,* edited J. Souletie *et al.* (Elsevier, Amsterdam, 1987), pp. 629–711.

[9]M. E. Glicksman, R. J. Schaefer, and J. D. Ayers, Metall. Trans. A **7**, 1747 (1976).

[10]E. Ben-Jacob, N. Goldenfeld, B. G. Kotliar, and J. S. Langer, Phys. Rev. Lett. **53**, 2110 (1984); J. S. Langer, Phys. Rev. A **33**, 435 (1986); J. S. Langer and D. C. Hong, *ibid.* **34**, 1462 (1986).

[11]The selection is dealt with numerically by D. I. Meiron, Phys. Rev. A **33**, 2704 (1986); D. A. Kessler, J. Koplik, and H. Levine, *ibid.* **33**, 3352 (1986). Analytical work is done by P. Pelcé and Y. Pomeau, Stud. Appl. Math. **74**, 245 (1986); A. Barbieri, D. C. Hong, and J. S. Langer, Phys. Rev. A **35**, 1802

(1987); M. Ben-Amar and Y. Pomeau, Europhys. Lett. **2**, 307 (1986). See also D. Kessler J. Koplik, and H. Levine, in *Patterns, Defects and Microstructures in Nonequilibrium Systems,* edited by D. Walgraet (Nijhoff, Dordrecht, Holland, 1986). Analytical work at high undercooling is done by, B. Caroli, C. Caroli, B. Roulet, and J. S. Langer, Phys. Rev. A **33**, 442 (1986); A. Barbieri, Phys. Rev. A **36**, 3340 (1987).

[12]Y. Saito, G. Goldbeck-Wood, and H. Müller-Krumbhaar, Phys. Rev. Lett. **58**, 1541 (1987).

[13]H. Honjo, S. Ohta, and Y. Sawada, Phys. Rev. Lett. **55**, 841 (1985). Tip oscillation of a given dendrite has also been observed in directional solidification, L. R. Morris and W. C. Winegard, J. Cryst. Growth **1**, 245 (1967).

[14]S.-C. Huang and M. E. Glicksman, Acta Metall. **29**, 701 (1981); **29**, 717 (1981); M. E. Glicksman, Mater. Sci. Eng. **65**, 45 (1984).

[15]A. Dougherty, P. D. Kaplan, and J. P. Gollub, Phys. Rev. Lett. **58**, 1652 (1987).

[16]W. W. Mullins and R. F. Sekerka, J. Appl. Phys. **34**, 323 (1963); **35**, 444 (1964). See also Ref. 1.

[17]For a careful discussion of the underlying assumptions and limitations of the BLM see W. van Sarloos and J. D. Weeks, Phys. Rev. Lett. **55**, 1685 (1985); J. D. Weeks and W. van Sarloos (unpublished).

[18]See, for example, R. F. Sekerka, in *Interfacial Aspects of Phase Transformations,* edited by B. Mutaftschiev (Reidel, Dordrecht, Holland, 1982), pp. 489–508.

[19]For experimental demonstration of the role of anisotropy see E. Ben-Jacob, R. Godbey, N. D. Goldenfeld, J. Koplik, H. Levine, T. Mueller, and L. M. Sander, Phys. Rev. Lett. **55**, 1315 (1985).

[20]G. Goldbeck, thesis, Rheinisch-Westfälischen Technischen Hochschule, 1986; H. Müller-Krumbhaar, G. Goldbeck, and Y. Saito, *Proceedings of the OJI Seminar on Crystal Morphology and Growth Units, August, 1985, Zao Hot Springs, Yamagata, Japan,* edited by I. Sunagawa (TERRA, Tokyo, 1988).

[21]J. S. Langer, R. F. Sekerka, and T. Fujioka, J. Cryst. Growth **44**, 414 (1978). Sidebranching of dendrites has also been observed during solidification of ^{4}He in J. P. Franck and J. Jung, J. Low Temp. Phys. **64**, 165 (1986). Using the values of L, C_v, and d_0 which Franck and Jung estimate gives $L^2 d_0^3 / C_v k_B$ on the order of 10^2. Thus by the estimate in Sec. III, thermal fluctuations again appear adequate to trigger sidebranching. Also, at lower undercooling, smooth fingers without sidebranches are reported. This is consistent with the behavior described in Sec. IV where sidebranching moves back from the tip as the undercooling is reduced. Note, however, that the presence of walls can also stabilize sidebranching and this may account for the observation of smooth fingers as the undercooling is reduced and as the size of the fingers increases.

[22]J. P. Gollub (private communication).

[23]J. S. Langer and H. Müller-Krumbhaar, Phys. Rev. A **27**, 499 (1983).

[24]See, for example, F. Heslot and A. Libchaber, Phys. Scr. **T9**, 126 (1985).

[25]R. J. Deissler, Physica (Utrecht) **18D**, 467 (1986).